

## Heterogeneous Catalysis

International Edition: DOI: 10.1002/anie.201910579  
German Edition: DOI: 10.1002/ange.201910579Engineering of Ruthenium–Iron Oxide Colloidal Heterostructures: Improved Yields in CO<sub>2</sub> Hydrogenation to Hydrocarbons

Aisulu Aitbekova, Emmett D. Goodman, Liheng Wu, Alexey Boubnov, Adam S. Hoffman, Arda Genc, Huikai Cheng, Lee Casalena, Simon R. Bare, and Matteo Cargnello\*

**Abstract:** Catalytic CO<sub>2</sub> reduction to fuels and chemicals is a major pursuit in reducing greenhouse gas emissions. One approach utilizes the reverse water-gas shift reaction, followed by Fischer–Tropsch synthesis, and iron is a well-known candidate for this process. Some attempts have been made to modify and improve its reactivity, but resulted in limited success. Now, using ruthenium–iron oxide colloidal heterodimers, close contact between the two phases promotes the reduction of iron oxide via a proximal hydrogen spillover effect, leading to the formation of ruthenium–iron core–shell structures active for the reaction at significantly lower temperatures than in bare iron catalysts. Furthermore, by engineering the iron oxide shell thickness, a fourfold increase in hydrocarbon yield is achieved compared to the heterodimers. This work shows how rational design of colloidal heterostructures can result in materials with significantly improved catalytic performance in CO<sub>2</sub> conversion processes.

## Introduction

CO<sub>2</sub> hydrogenation to hydrocarbons has received significant attention in the scientific community owing to the possibility of reducing emissions of this greenhouse gas while producing fuels and chemicals. A proposed process to achieve this result is a modified Fischer–Tropsch (FT) synthesis; in this, the reverse water-gas shift (RWGS) reaction first converts CO<sub>2</sub> into CO intermediate, which is further converted into hydrocarbons by the FT process (CO<sub>2</sub>-FT synthesis).<sup>[1]</sup> Instead of performing the two steps separately, it is often more convenient to incorporate them into a single reactor. However, there are several challenges associated with direct CO<sub>2</sub> conversion into hydrocarbons, including thermodynamic limitations and catalyst poisoning.<sup>[1]</sup> Effective

catalysts should be active for both RWGS and FT synthesis. Among many catalytic materials that have been investigated for this process, iron is a promising candidate because of its activity for both steps of the reaction and cheap price. It has been demonstrated that replacing CO with CO<sub>2</sub> in the reaction feed does not lead to significant changes in product distribution over iron catalysts, suggesting that the metal is effective for both the FT and CO<sub>2</sub>-FT synthesis.<sup>[2]</sup> Furthermore, recent studies have demonstrated that potassium-doped iron is effective for converting CO<sub>2</sub> directly to light olefins.<sup>[3]</sup> Unlike iron, other metals that are used for the FT synthesis, such as cobalt and ruthenium, predominantly perform CO<sub>2</sub> methanation.<sup>[2]</sup> For this reason, iron has been the subject of many investigations aimed at improving its performance for CO<sub>2</sub> hydrogenation. In order to improve the activity of iron-based catalysts, various metal promoters and alloys of iron with different metals have been studied. Particular attention has been paid to alloying iron with ruthenium owing to two main reasons: first, ruthenium is the most active FT metal, thus its addition is expected to increase conversion in iron-based systems; second, alloying iron with ruthenium results in a change in the electronic d-band structure that can give rise to distinct catalytic properties.<sup>[4]</sup>

The synthesis of promoted iron catalysts is usually performed via impregnation of a support using two metal salt precursors. However, such a preparation technique does not guarantee exclusive formation of uniform alloy nanoparticles. Instead, these bimetallic catalysts likely contain iron and ruthenium phases that are present both as alloys and separate nanoparticles of the individual metals.<sup>[4,5]</sup> It has been reported that reduction of alumina-impregnated ruthenium and iron salts leads to formation of both Fe/Ru alloys and segregated iron nanoparticles.<sup>[6]</sup> As a result, it is likely that the metals are present in various phases and oxidation states and that this heterogeneity can help explain the reported variability in the catalytic activity regarding the effects of ruthenium addition on FT activity of iron-based catalysts. For example, some studies show that the addition of Ru increases CO conversion and shifts product distribution from olefins towards heavier hydrocarbons,<sup>[4,5d,e]</sup> while others claim that Ru addition does not have significant effects on activity and selectivity.<sup>[5c]</sup> CO<sub>2</sub>-FT processes over ruthenium–iron catalysts have been studied to a significantly lesser extent; however, previous reports on this topic also presents conflicting results. Similar to the case of FT synthesis, while some reports show that Ru shifts the product distribution from shorter to longer chain hydrocarbons,<sup>[7]</sup> others do not observe significant effects of Ru promotion.<sup>[8]</sup> In this contribution, we

[\*] A. Aitbekova, E. D. Goodman, Dr. L. Wu, Prof. M. Cargnello  
Department of Chemical Engineering and SUNCAT Center for  
Interface Science and Catalysis, Stanford University  
443 Via Ortega, Stanford, CA, 94305 (USA)  
E-mail: mcargnello@stanford.edu

Dr. L. Wu, Dr. A. Boubnov, Dr. A. S. Hoffman, Dr. S. R. Bare  
Stanford Synchrotron Radiation Lightsource  
SLAC National Accelerator Laboratory  
2575 Sand Hill Rd., Menlo Park, CA, 94025 (USA)

Dr. A. Genc, Dr. H. Cheng, Dr. L. Casalena  
Thermo Fisher Scientific  
5350 NE Dawson Creek Dr., Hillsboro, OR, 97124 (USA)

Supporting information and the ORCID identification number(s) for the author(s) of this article can be found under:  
<https://doi.org/10.1002/anie.201910579>.

investigate the effect of ruthenium on iron-based systems for the CO<sub>2</sub>-FT process by utilizing well-defined ruthenium–iron oxide colloidal heterodimers and core–shell structures. We demonstrate that the close contact between the two phases promotes the reduction of iron oxide via a proximal hydrogen spillover effect, enabling the formation of the active iron/iron carbide phase for the reaction at significantly lower temperatures than in iron oxide catalysts. We also observed the transformation of heterodimers into core–shell structures owing to the encapsulation of ruthenium by iron oxide upon reductive pretreatment. Furthermore, by engineering core–shell structures with a thin iron oxide shell, we achieved a fourfold increase in hydrocarbon yield compared to the heterodimers.

## Results and Discussion

The heterodimers were synthesized using a seed-mediated colloidal approach. This method leads to structures where ruthenium and iron oxide nanoparticles are located in direct contact with each other by way of shared crystallographic facets. Ru nanoparticle seeds (4.8 nm average particle size) were obtained through thermal decomposition of Ru<sub>3</sub>(CO)<sub>12</sub> in oleylamine using a previously reported procedure.<sup>[9]</sup> Iron oxide nanoparticles (13.1 nm average particle size) were then grown onto the Ru seeds by addition of Fe(CO)<sub>5</sub> and its subsequent decomposition at 300 °C in a mixture of 1-octadecene, oleic acid, and oleylamine, optimizing previously reported synthesis procedures.<sup>[10]</sup> A detailed synthesis procedure is given in the Supporting Information. Representative transmission electron microscopy (TEM) images (Figure 1 a) demonstrate the formation of the heterodimers, with each higher contrast spherical Ru nanoparticle in direct contact

with a lower contrast iron oxide nanoparticle. Very few isolated ruthenium or iron oxide nanoparticles were observed. Lattice fringe analysis of the iron oxide phase identified distances between two adjacent planes to be 0.294 nm and 0.485 nm (Supporting Information, Figure S1), which can be assigned to (220) and (111) planes of inverse spinel structured Fe<sub>3</sub>O<sub>4</sub>, respectively.<sup>[10a]</sup> Therefore, the iron oxide in the as-synthesized heterodimers is being present as Fe<sub>3</sub>O<sub>4</sub>, as ascertained by previous studies.<sup>[10a,c]</sup> It is hypothesized that the formation of heterodimers is obtained through deposition of metallic iron first, which then promotes further decomposition of the iron precursor and its oxidation to iron oxide material grown epitaxially.<sup>[11]</sup> The heterodimers were then deposited onto  $\gamma$ -Al<sub>2</sub>O<sub>3</sub> support, and the organic ligands removed using a fast calcination treatment.<sup>[12]</sup> The nominal weight loading in terms of total metal content (Ru + Fe) was set to 1 wt % with respect to the support. The heterodimer structure was maintained after deposition and calcination, as demonstrated by high-angle annular dark field scanning transmission electron microscopy (HAADF-STEM) imaging and energy-dispersive X-ray scattering (EDS) maps of the catalyst after calcination (Figure 1 c–f). These images confirm that the heterodimer nature of the materials is maintained after the calcination process to remove ligands used during the synthesis. Furthermore, X-ray absorption spectroscopy (XAS) characterization of the supported sample after the fast calcination at 700 °C showed that the Ru was partially oxidized (as evidenced by a small Ru–O scattering path in the EXAFS) and the Fe<sub>3</sub>O<sub>4</sub> was oxidized into  $\gamma$ -Fe<sub>2</sub>O<sub>3</sub> (Supporting Information, Table S1, Figure S2).

The catalytic activity of the heterodimer catalyst was compared to various control catalysts to determine how the interaction of ruthenium and iron oxide phases affects their properties. The three control samples were Ru/Al<sub>2</sub>O<sub>3</sub>, Fe<sub>2</sub>O<sub>3</sub>/

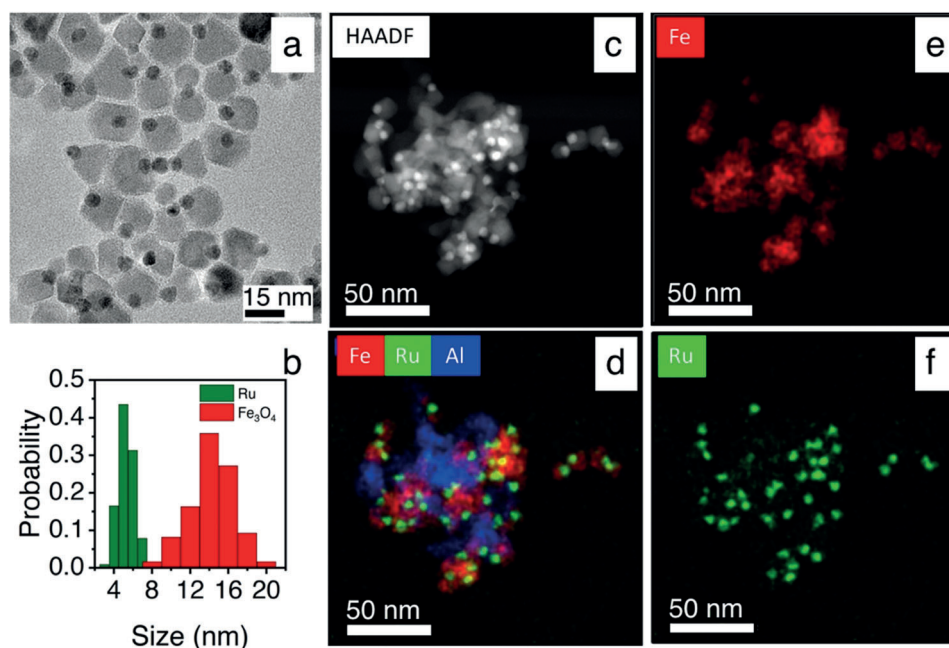


**Figure 1.** a), b) Representative TEM image of as-synthesized Ru/Fe<sub>3</sub>O<sub>4</sub> heterodimers and corresponding particle size distributions. c) Representative HAADF-STEM image and d)–f) EDS maps of the Ru/Fe<sub>2</sub>O<sub>3</sub>/Al<sub>2</sub>O<sub>3</sub> catalyst after calcination.



$\text{Al}_2\text{O}_3$  and a physical mixture of these two. The nominal weight loading in terms of total metal content was 1 wt % for all control samples. The ruthenium nanoparticles for the Ru/ $\text{Al}_2\text{O}_3$  sample were from the same batch as the seeds employed for the synthesis of the heterodimers. Iron oxide nanoparticles were synthesized through thermal decomposition of  $\text{Fe}(\text{acac})_3$  in a mixture of benzyl ether and oleylamine (Supporting Information, Figure S3).<sup>[13]</sup> The control samples were also subjected to the same fast calcination treatment to remove organic ligands. X-ray absorption near-edge spectra (XANES) characterization was performed on the supported iron oxide sample after the fast calcination (Supporting Information, Figure S2). The slightly lower overall intensity of the  $\gamma\text{-Fe}_2\text{O}_3$  standard was due to the fact that the spectrum was collected at a different facility. This difference, however, did not affect the identification of the iron state in the catalyst showing that the iron was being present exclusively as  $\gamma\text{-Fe}_2\text{O}_3$ .

In a first catalytic test, all catalysts were reduced at 300 °C in pure  $\text{H}_2$  and tested for  $\text{CO}_2$  hydrogenation at 6 bar and 300 °C in a 3:1 mixture of  $\text{H}_2/\text{CO}_2$ . Catalytic measurements were performed under differential conditions with  $\text{CO}_2$  conversion of less than 1 % by adjusting the gas hourly space velocity (GHSV). The catalytic results are reported in Figure 2. Equations used to calculate selectivity can be found in the Supporting Information. In this low conversion regime, all catalysts produced carbon monoxide and methane as the dominant products, in agreement with previous works.<sup>[3]</sup> The  $\text{Fe}_2\text{O}_3/\text{Al}_2\text{O}_3$  catalyst produced almost exclusively CO, the Ru/ $\text{Al}_2\text{O}_3$  catalyst formed  $\text{CH}_4$  with about 70% selectivity,

and their physical mixture resulted in an intermediate selectivity between the two. However, among all the catalysts tested, only the heterodimer Ru/ $\text{Fe}_2\text{O}_3/\text{Al}_2\text{O}_3$  sample produced hydrocarbons and methanol. The fact that the physical mixture only produced CO and  $\text{CH}_4$ , while the Ru/ $\text{Fe}_2\text{O}_3/\text{Al}_2\text{O}_3$  heterodimer catalyst formed hydrocarbons (Figure 2a) demonstrates the importance of proximity between ruthenium and iron oxide phases. We set out to investigate the reason for the observed differences in the catalytic activity between Ru/ $\text{Fe}_2\text{O}_3/\text{Al}_2\text{O}_3$  and  $\text{Fe}_2\text{O}_3/\text{Al}_2\text{O}_3$ .

Characterization of iron catalysts with ex situ techniques provides only limited information, as Fe is known to become oxidized by oxygen when exposed to air precluding accurate characterization of the active phase.<sup>[5b,14]</sup> Therefore, we studied our materials with in situ XAS to monitor changes in the oxidation state of iron and ruthenium in the Ru/ $\text{Fe}_2\text{O}_3/\text{Al}_2\text{O}_3$  heterodimer and  $\text{Fe}_2\text{O}_3/\text{Al}_2\text{O}_3$  catalysts. In situ Ru K-edge XANES and EXAFS data of the Ru/ $\text{Fe}_2\text{O}_3/\text{Al}_2\text{O}_3$  sample after the reductive pretreatment in a flow of hydrogen show that the partially oxidized ruthenium completely reduces to metallic state (Supporting Information, Figure S4, Table S1). Figure 3a,b and the Supporting Information, Tables S2, S3 report results and quality of linear combination fitting (LCF) during the reductive pretreatment using relevant standards (Supporting Information, Figures S5). Figure 3c,d shows corresponding in situ Fe K-edge XANES of the Ru/ $\text{Fe}_2\text{O}_3/\text{Al}_2\text{O}_3$  and  $\text{Fe}_2\text{O}_3/\text{Al}_2\text{O}_3$  samples. Representative LCF data and fits are presented in the Supporting Information, Figures S6, S7. The initial iron phase after the fast calcination for both catalysts is  $\gamma\text{-Fe}_2\text{O}_3$  (Supporting Information, Figure S2). However, the temperature-dependent evolution of the Fe oxidation state varies dramatically between the two samples. Heated in pure  $\text{H}_2$ , both samples first reduce from  $\gamma\text{-Fe}_2\text{O}_3$  to  $\text{Fe}_3\text{O}_4$ , although this reduction occurs at a significantly lower temperature for the heterodimer sample compared to the  $\text{Fe}_2\text{O}_3/\text{Al}_2\text{O}_3$  catalyst. For the heterodimer sample, this first reduction starts at 50 °C and is complete by 100 °C, while the  $\text{Fe}_2\text{O}_3/\text{Al}_2\text{O}_3$  sample starts reducing at 100 °C and finishes at about 230 °C. A more important difference between the two samples becomes evident after this first phase transformation. In the Ru/ $\text{Fe}_2\text{O}_3/\text{Al}_2\text{O}_3$  heterodimer catalyst, the iron phase completely transitions to metallic iron at about 300 °C. Instead, the  $\text{Fe}_2\text{O}_3/\text{Al}_2\text{O}_3$  slowly transitions from  $\text{Fe}_3\text{O}_4$  to FeO, before metallic iron starts to form. This final reduction is not complete until 500 °C. In other words, in the Ru/ $\text{Fe}_2\text{O}_3/\text{Al}_2\text{O}_3$  catalyst, complete reduction of  $\text{Fe}_2\text{O}_3$  happens at a temperature 200 °C lower than the  $\text{Fe}_2\text{O}_3$  alone.

There is no consensus regarding the nature of active sites of  $\text{CO}_2$ -FT/FT iron catalysts. However, at least three phases of iron have been identified as possible active sites under reaction conditions: several states of iron oxides and iron carbides, and metallic iron.<sup>[14]</sup> There is general agreement that under reaction conditions these various phases co-exist and their relative concentrations undergo dynamic changes.<sup>[14]</sup> Among them, iron carbides are thought to be crucial for the formation of hydrocarbons,<sup>[15]</sup> while iron oxides have been identified as being active for WGS/RWGS reactions.<sup>[3a]</sup> Thus, since the pretreatment of the  $\text{Fe}_2\text{O}_3/\text{Al}_2\text{O}_3$  catalyst was

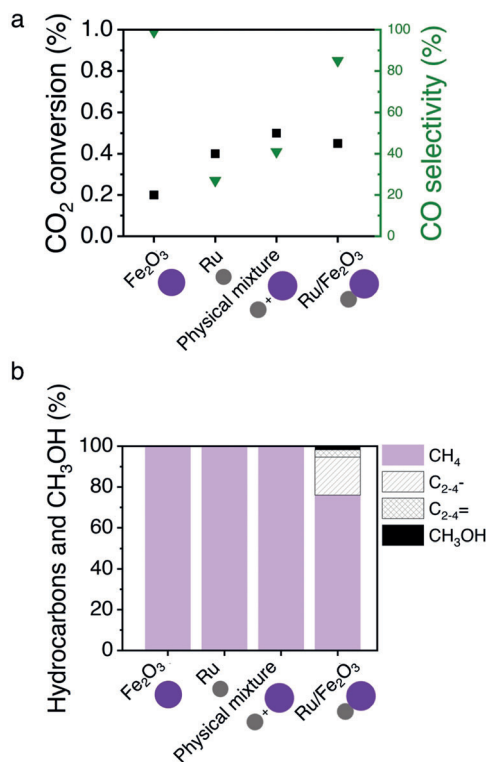


**Figure 2.** a)  $\text{CO}_2$  conversion (black ■) and CO selectivity (green ▼); b) hydrocarbon and methanol distributions.

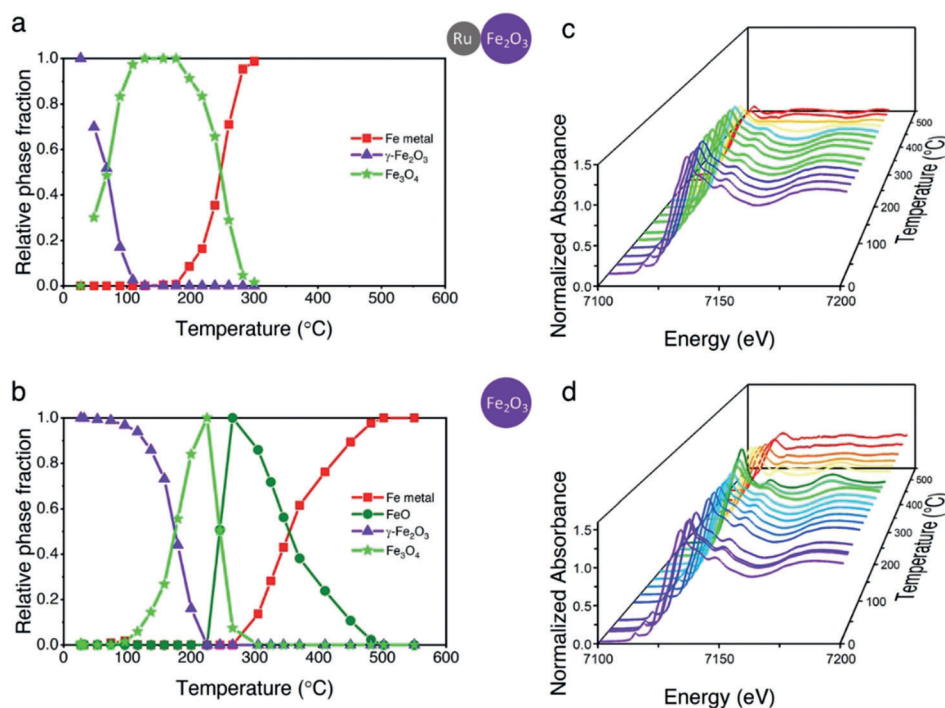


**Figure 3.** a),b) Linear combination fitting of the in situ Fe K-edge XANES spectra showing the relative fraction of different Fe phases found in the heterodimer and  $\text{Fe}_2\text{O}_3/\text{Al}_2\text{O}_3$  catalysts, respectively; c),d) In situ Fe K-edge XANES spectra used in the linear combination fitting for the heterodimer and  $\text{Fe}_2\text{O}_3/\text{Al}_2\text{O}_3$  catalysts, respectively.

performed at 300°C, and at this temperature the catalyst is comprised mostly FeO phase, then this is an indication that the FeO phase is responsible for the observed RWGS reactivity of this catalyst. To confirm that the formation of metallic iron is a prerequisite for hydrocarbon synthesis, we reduced the  $\text{Fe}_2\text{O}_3/\text{Al}_2\text{O}_3$  sample at 550°C and measured its catalytic activity again. After this high-temperature reduction, the sample indeed produced hydrocarbons and methanol with a product distribution similar to that of the heterodimers reduced at 300°C (Supporting Information, Figure S8). Similar catalytic selectivity of the heterodimers reduced at 300°C and the iron oxide sample reduced at 550°C suggest that the role of ruthenium is to promote the reduction of iron oxide to the active iron phase. However, TEM characterization of the post-catalysis sample showed that there was severe sintering of the nanoparticles with an increase in their average size from 6.0 nm to 15.1 nm as a result of the high-temperature reduction treatment (Supporting Information, Figure S9). The activity of the catalyst after 550°C reduction decreased compared to the heterodimer sample reduced at 300°C, when normalized by mass of total metal. However, GHSV was adjusted to maintain similar conversion levels (<1%) for both catalysts to accurately compare selectivity data (Supporting Information, Figure S8). We realize that mass normalization is not a fair normalization technique given the nature of our materials, however, we did not investigate differences in intrinsic activity in detail owing to challenges associated with comparing activity of bimetallic and monometallic systems nicely described in previous studies.<sup>[4]</sup>

The profound differences in the catalytic behavior of all samples reduced at 300°C are, therefore, related to the reduction of the iron phase in the heterodimers at lower temperatures, driven by the proximity of iron oxide to the metallic Ru nanoparticles in the sample. It is well-established that noble metals promote the reduction of transition-metal oxides via hydrogen spillover effects.<sup>[16]</sup> Activation barriers for hydrogen activation on metals are usually lower compared to metal oxides.<sup>[16]</sup> When metals activate and split molecular hydrogen, hydrogen atoms spill onto the oxide phase through hydroxyl groups present on its surface, promoting the reduction of the transition metal to a lower oxidation state and/or to the metallic phase. The hydrogen spillover effect depends critically on the metal/metal oxide pair combination, and on the distance between the two phases.<sup>[16]</sup> On alumina, which is the support used in our study, the critical distance was found to be approximately 15 nm.<sup>[16]</sup> Therefore, we attribute the improved catalytic performance of the heterodimers to a greater extent of reduction of the iron oxide, promoted by the proximity of the metallic ruthenium phase via hydrogen spillover. Despite a plethora of studies on ruthenium–iron oxide systems for  $\text{CO}_2$ -FT/FT synthesis, promotion of iron oxide reduction by ruthenium and detailed evolution of iron oxide phases upon reduction have not been reported before. This effect cannot be activated in the physical mixture because of the far distance between ruthenium and iron oxide phases (micrometers) or in the sample with only iron oxide phase because of the absence of metallic ruthenium that can activate hydrogen.



Further HAADF-STEM characterization of the Ru/Fe<sub>2</sub>O<sub>3</sub>/Al<sub>2</sub>O<sub>3</sub> heterodimer sample after catalysis demonstrated an unexpected structural transformation of the catalyst. Here, we observed the presence of a core-shell structure, with a high-contrast core surrounded by a lower-contrast shell material of the nanoparticles supported on alumina (Figure 4). EDS-mapping suggested that the core material is mostly composed of Ru, encapsulated by Fe and C, whereas the shell mostly of Fe and O. These maps suggest that ruthenium was encapsulated by the iron phase during the reduction and/or catalytic reaction. EDS line scans (Supporting Information, Figure S10) and EDS tomography (Supporting Information, Videos S1, S2) of the fresh and the post-catalysis heterodimer sample further demonstrate the core-shell nature of the nanoparticles in the spent catalyst.

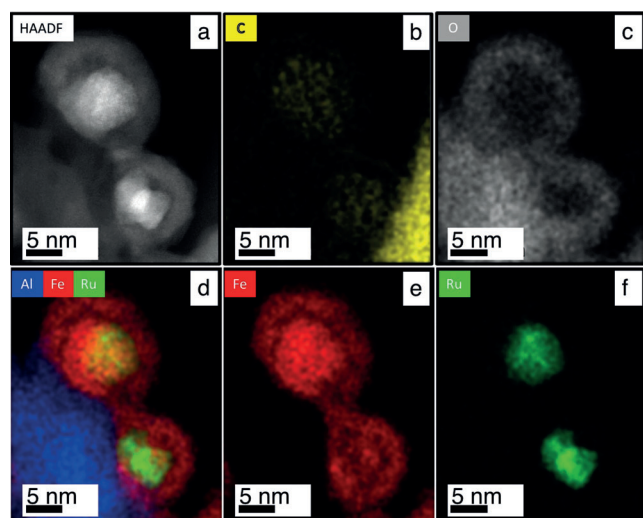


**Figure 4.** a) Representative HAADF-STEM image and b) to f) energy dispersive X-ray spectroscopy maps of b) C, c) O, d) superposition of Al, Fe, and Ru, e) Fe, and f) Ru in the post-catalysis heterodimer sample.

To understand whether the encapsulation occurs during the reductive pretreatment or during reaction, we reduced the heterodimers at 300 °C and characterized the sample using TEM. These micrographs indicate the presence of thin overlayers of an iron phase, in this case iron oxide (Supporting Information, Figure S11). This observed behavior is consistent with a strong metal-support interaction effects between a reducible oxide and Group 8 noble metals, where the reduced oxide phase covers the surface of a supported metal as a result of more favorable surface energy.<sup>[17]</sup> Upon reduction of surface  $\gamma$ -Fe<sub>2</sub>O<sub>3</sub> to FeO<sub>x</sub>, the latter migrates on the ruthenium metal surface, leading to encapsulation of the ruthenium. Such transformation of ruthenium-iron oxide heterodimers into core-shell structures has not been reported before.

We further studied the Ru/Fe<sub>2</sub>O<sub>3</sub>/Al<sub>2</sub>O<sub>3</sub> sample by modeling in situ Ru K-edge EXAFS data of the fresh, reduced, and post-catalysis samples. The EXAFS data are shown in the Supporting Information, Figures S12, S13 and the numerical results of the modeling for each sample are presented in the

Supporting Information, Table S1. The best fit model to the EXAFS data confirms that the fresh catalyst comprises both metallic Ru and Ru oxide, and the coordination numbers are consistent with the Ru being present as nanoparticles. However, after reduction, the Ru–O scattering path at 2.01 Å disappeared, indicating that the sample completely reduced to metallic Ru. At the same time, while the reduced and the post-catalysis samples mostly consist of one dominant contribution owing to Ru–Ru at 2.66 Å, the two samples have non-negligible contributions at 2.58 Å (Supporting Information, Figures S12–S14, Table S1). Previous studies identified that this distance corresponds to the Ru–Fe scattering path.<sup>[18]</sup> Thus, the fact that we see appearance of Ru–Fe contribution in the reduced and the post-catalysis samples is consistent with Ru encapsulation by Fe, in agreement with the EDS characterization. The EDS maps in Figure 4 suggest that while the core mostly comprised of metallic Ru, the presence of the Ru–Fe contribution in the EXAFS modelling suggests formation of alloying of Ru surface layers with Fe. While XANES at the Ru edge does not show significant differences between the reduced catalyst and metallic Ru, the EXAFS analysis clearly indicates the appearance of the Ru–Fe contribution after reduction of the catalyst (Supporting Information, Figures S12–S14, Table S1). We believe that the interaction between Ru and Fe is only pronounced in EXAFS because it is a fraction of surface Ru atoms that would interact with Fe, and the XANES spectrum at the Ru K-edge is relatively insensitive to charge transfer (s→p). In a Ru nanoparticle of an average size of 4.8 nm, the fraction of surface atoms is about 16%. This value is consistent with the obtained Ru–Fe coordination numbers (Supporting Information, Table S1). EXAFS fitting at the Fe edge, however, did not show Fe–Ru contribution in the reduced sample probably owing to the even smaller fraction of Fe interacting with Ru (ca. 3%) in the core-shell structure.

We also observed similar core-shell structures in the pure iron oxide sample after catalysis (Supporting Information, Figure S9). Lattice fringe analysis clearly demonstrates that the shells are crystalline, with lattice constants corresponding to either  $\gamma$ -Fe<sub>2</sub>O<sub>3</sub> or Fe<sub>3</sub>O<sub>4</sub> (Supporting Information, Figure S9). The presence of an iron oxide shell evidenced by (S)TEM and EDS in the spent catalysts is likely the result of oxidation following exposure to air rather than a realistic representation of the catalyst structure under reaction conditions. Indeed, in situ Fe K-edge XANES showed that the heterodimer sample predominantly consisted of metallic iron and iron carbide phases with no observable contribution from  $\gamma$ -Fe<sub>2</sub>O<sub>3</sub> (Supporting Information, Figure S15). However, during the in situ experiments we observed that upon cool down in the reaction mixture, the contribution owing to metallic iron decreased, while that of  $\gamma$ -Fe<sub>2</sub>O<sub>3</sub> increased (Supporting Information, Figure S15). Thus, we surmise that the active phase of the catalyst consists mainly of metallic iron and iron carbide phases which, upon exposure to air, oxidize and form an iron oxide shell. This result is easily understood given the susceptibility of iron to oxidation. EDS maps (Figure 4) are consistent with this claim since we found a non-negligible carbon signal arising from the core of the nanostructures (Figure 4c). The overall characterization by com-

binning XAS and (S)TEM provides an idea of the challenges associated in determining active phases and the need to combine in situ tools for a full description of catalyst structure.

Our experiments suggest that once ruthenium promotes the reduction of iron oxide and a core-shell structure is formed, the catalytic activity of the heterodimers is similar to that of pure iron oxide. This result can be explained by the presence of a relatively thick shell of iron (4.3 nm on average) that dominates the activity. However, electronic promotion of the iron phase can be obtained if the iron oxide shell thickness is decreased. Based on this knowledge, we prepared Ru/FeO<sub>x</sub> core-shell nanoparticles with an average shell thickness of 1.2 nm directly from colloidal synthesis (Figure 5a) and deposited them onto the same Al<sub>2</sub>O<sub>3</sub> support as for the heterodimers. EDS line scans confirmed the presence of iron in the shell and ruthenium in the core (Supporting Information, Figure S16). The catalyst was reduced in pure hydrogen at 300 °C and catalytic activity was tested under differential conditions. Interestingly, the core-shell nanoparticles with much thinner shell made significantly more hydrocarbons compared to the heterodimers at similar conversion, demonstrating a twofold and fourfold increase in the selectivity to hydrocarbons and the hydrocarbon yield, respectively, compared to the heterodimers (Figure 5b). TEM analysis of the post-catalysis sample showed no sintering and no changes of the supported core-shell structures (Supporting Information, Figure S17). We hypothesize that because of the thin shell,

electronic interactions between the Ru core and iron shell become stronger and, thus, affect the catalytic selectivity of the CO<sub>2</sub> hydrogenation products. The catalytic activity and selectivity of the two samples was also compared at higher CO<sub>2</sub> conversion (Supporting Information, Figure S18).

Finally, we demonstrate that the benefits of phase proximity in the heterodimer structures are not limited to ruthenium, and provide a general framework for the development of more efficient heterogeneous catalysts using colloidal nanomaterial design. To achieve this goal, we synthesized Pd/FeO<sub>x</sub> heterodimers in a straightforward extension of the Ru/FeO<sub>x</sub> synthesis process. These nanoparticles were deposited onto alumina and activated by reduction at 300 °C as previously described for the ruthenium counterpart, and their performance for CO<sub>2</sub>-FT examined under the same conditions (Supporting Information, Figure S19). The catalyst produced hydrocarbons from CO<sub>2</sub>-FT, thus supporting the promotion mechanism of reduction of iron oxide by noble metals via hydrogen spillover. However, Pd/FeO<sub>x</sub>/Al<sub>2</sub>O<sub>3</sub> had higher selectivity to methanol probably due to either alloying of Pd and Fe metals or partially exposed Pd surface. TEM characterization of the fresh and post-catalysis samples (Supporting Information, Figure S19) suggests Pd encapsulation within Fe, consistent with our ruthenium-iron oxide results.

## Conclusion

In conclusion, we demonstrated a synergistic effect in ruthenium-iron oxide heterodimer catalysts where promotion of the iron phase for CO<sub>2</sub> hydrogenation to hydrocarbons is realized through hydrogen activation and spillover from the proximal ruthenium phase to the iron component. Additionally, we observed the transformation of heterodimers into ruthenium-iron core-shell structures owing to the encapsulation of ruthenium by iron oxide upon reductive pretreatment. Thanks to this knowledge, we realized core-shell structures with a fourfold increase in the hydrocarbon yield compared to the initial heterodimers, thus designing an efficient catalyst for CO<sub>2</sub> conversion to hydrocarbons. This work is the first example of the synthesis and application of ruthenium-iron oxide heterodimers and core-shell structures for CO<sub>2</sub>-FT. The well-defined structure of our starting materials enabled us to study the cooperative mechanism of ruthenium promotion and its implication on the catalytic performance.

## Acknowledgements

We gratefully acknowledge support from the Stanford Precourt Institute for Energy through a seed grant. M.C. acknowledges additional support from the School of Engineering at Stanford University and from a Terman Faculty Fellowship. A.A. acknowledges support from a Stanford Graduate Fellowship (SGF) and an EDGE fellowship. E.D.G. acknowledges support from the National Science Foundation Graduate Research Fellowship under Grant DGE-1656518.

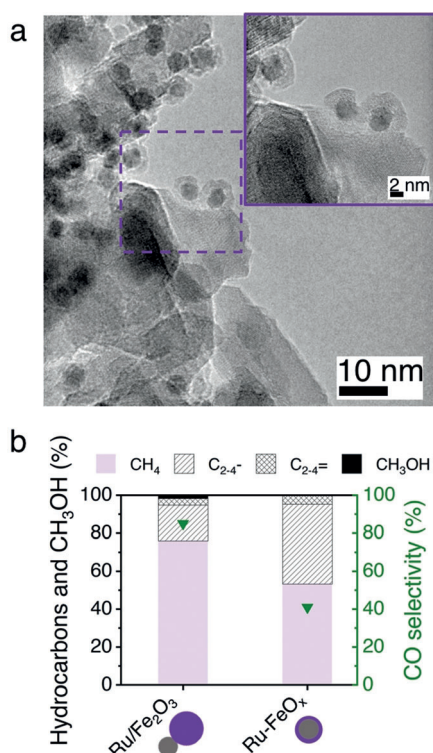


**Figure 5.** a) Representative TEM image of core-shell Ru-FeO<sub>x</sub> nanoparticles deposited on the Al<sub>2</sub>O<sub>3</sub> support and b) hydrocarbon and methanol distributions and CO selectivity over the Ru/Fe<sub>2</sub>O<sub>3</sub> heterodimers and Ru-FeO<sub>x</sub> core-shell nanoparticles reduced at 300 °C.



Part of this work was performed at the Stanford Nano Shared Facilities (SNSF), supported by the National Science Foundation under award ECCS-1542152. Part of this work was also performed at Stanford Synchrotron Radiation Lightsource (SSRL) of SLAC National Accelerator Laboratory and use of the SSRL is supported by the U.S. Department of Energy, Office of Science, Office of Basic Energy Sciences under Contract No. DE-AC02-76SF00515 and by CO-ACCESS supported by the U.S. Department of Energy, Office of Basic Energy Sciences, Chemical Sciences, Geosciences & Biosciences Division.

### Conflict of interest

The authors declare no conflict of interest.

**Keywords:** CO<sub>2</sub> hydrogenation · hydrocarbons · hydrogen spillover · iron · ruthenium

- [1] M. D. Porosoff, B. Yan, J. G. Chen, *Energy Environ. Sci.* **2016**, *9*, 62–73.
- [2] T. Riedel, M. Claeys, H. Schulz, G. Schaub, S.-S. Nam, K.-W. Jun, M.-J. Choi, G. Kishan, K.-W. Lee, *Appl. Catal. A* **1999**, *186*, 201–213.
- [3] a) C. G. Visconti, M. Martinelli, L. Falbo, A. Infantes-Molina, L. Lietti, P. Forzatti, G. Iaquaniello, E. Palo, B. Picutti, F. Brignoli, *Appl. Catal. B* **2017**, *200*, 530–542; b) R. Sathawong, N. Koizumi, C. Song, P. Prasassarakich, *Catal. Today* **2015**, *251*, 34–40.
- [4] A. Meffre, V. Iablokov, Y. Xiang, R. Barbosa, P. F. Fazzini, V. Kelsen, N. Kruse, B. Chaudret, *Catal. Lett.* **2015**, *145*, 373–379.
- [5] a) G. L. Ott, T. Fleisch, W. N. Delgass, *J. Catal.* **1980**, *65*, 253–262; b) A. M. van der Kraan, R. C. H. Nonnekens, F. Stoop, J. W. Niemantsverdriet, *Appl. Catal.* **1986**, *27*, 285–298; c) M. C. Bahome, L. L. Jewell, K. Padayachy, D. Hildebrandt, D. Glasser, A. K. Datye, N. J. Coville, *Appl. Catal. A* **2007**, *328*, 243–251; d) G. L. Ott, T. Fleisch, W. N. Delgass, *J. Catal.* **1979**, *60*, 394–403; e) F. J. Berry, L. Liwu, W. Chengyu, T. Renyuan, Z. Su, L. Dongbai, *J. Chem. Soc. Faraday Trans. 1* **1985**, *81*, 2293–2305; f) S. Li, S. Krishnamoorthy, A. Li, G. D. Meitzner, E. Iglesias, *J. Catal.* **2002**, *206*, 202–217.
- [6] K. R. Kannan, G. U. Kulkarni, C. N. R. Rao, *Catal. Lett.* **1992**, *14*, 149–163.
- [7] S.-C. Lee, J.-H. Jang, B.-Y. Lee, J.-S. Kim, M. Kang, S.-B. Lee, M.-J. Choi, S.-J. Choung, *J. Mol. Catal. A* **2004**, *210*, 131–141.
- [8] F. Jiang, B. Liu, S. Geng, Y. Xu, X. Liu, *Catal. Sci. Technol.* **2018**, *8*, 4097–4107.
- [9] A. Aitbekova, L. Wu, C. J. Wrasman, A. Boubnov, A. S. Hoffman, E. D. Goodman, S. R. Bare, M. Cargnello, *J. Am. Chem. Soc.* **2018**, *140*, 13736–13745.
- [10] a) H. Yu, M. Chen, P. M. Rice, S. X. Wang, R. L. White, S. Sun, *Nano Lett.* **2005**, *5*, 379–382; b) C. Xu, J. Xie, D. Ho, C. Wang, N. Kohler, E. G. Walsh, J. R. Morgan, Y. E. Chin, S. Sun, *Angew. Chem. Int. Ed.* **2008**, *47*, 173–176; *Angew. Chem.* **2008**, *120*, 179–182; c) C. Wang, H. Daimon, S. Sun, *Nano Lett.* **2009**, *9*, 1493–1496.
- [11] L. Carbone, P. D. Cozzoli, *Nano Today* **2010**, *5*, 449–493.
- [12] M. Cargnello, C. Chen, B. T. Diroll, V. V. T. Doan-Nguyen, R. J. Gorte, C. B. Murray, *J. Am. Chem. Soc.* **2015**, *137*, 6906–6911.
- [13] Z. Xu, C. Shen, Y. Hou, H. Gao, S. Sun, *Chem. Mater.* **2009**, *21*, 1778–1780.
- [14] M. D. Shroff, D. S. Kalakkad, K. E. Coulter, S. D. Kohler, M. S. Harrington, N. B. Jackson, A. G. Sault, A. K. Datye, *J. Catal.* **1995**, *156*, 185–207.
- [15] P. Wang, W. Chen, F.-K. Chiang, A. I. Dugulan, Y. Song, R. Pestman, K. Zhang, J. Yao, B. Feng, P. Miao, W. Xu, E. J. M. Hensen, *Sci. Adv.* **2018**, *4*, eaau2947.
- [16] W. Karim, C. Spreafico, A. Kleibert, J. Gobrecht, J. VandeVondele, Y. Ekinci, J. A. van Bokhoven, *Nature* **2017**, *541*, 68.
- [17] a) S. J. Tauster, *Acc. Chem. Res.* **1987**, *20*, 389–394; b) S. J. Tauster, S. C. Fung, R. T. K. Baker, J. A. Horsley, *Science* **1981**, *211*, 1121–1125; c) S. Zhang, P. N. Plessow, J. J. Willis, S. Dai, M. Xu, G. W. Graham, M. Cargnello, F. Abild-Pedersen, X. Pan, *Nano Lett.* **2016**, *16*, 4528–4534; d) S. J. Tauster, S. C. Fung, R. L. Garten, *J. Am. Chem. Soc.* **1978**, *100*, 170–175.
- [18] Y. Yang, F. Yang, C.-J. Sun, H. Zhao, S. Hao, D. E. Brown, J. Zhang, Y. Ren, *RSC Adv.* **2017**, *7*, 6818–6826.

Manuscript received: August 19, 2019

Accepted manuscript online: September 23, 2019

Version of record online: ■ ■ ■ ■ ■ ■ ■ ■ ■ ■

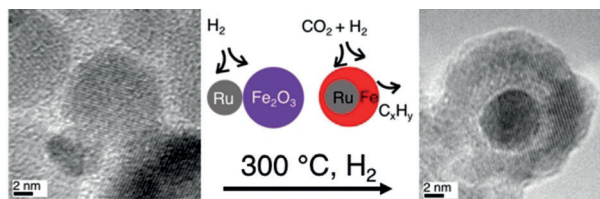


## Research Articles

## Heterogeneous Catalysis

A. Aitbekova, E. D. Goodman, L. Wu,  
A. Boubnov, A. S. Hoffman, A. Genc,  
H. Cheng, L. Casalena, S. R. Bare,  
M. Cargnello\*     

Engineering of Ruthenium–Iron Oxide Colloidal Heterostructures: Improved Yields in CO<sub>2</sub> Hydrogenation to Hydrocarbons



**Ruthenium promotes** reduction of iron oxide in ruthenium–iron oxide heterodimers by a proximal hydrogen spillover effect, leading to the formation of ruthenium–iron core–shell structures active for CO<sub>2</sub> hydrogenation to hydrocarbons.

Tuning the shell thickness leads to a four-fold increase in hydrocarbon yield.